BAYWRF: a convection-resolving, present-day climatological atmospheric dataset for Bavaria

Emily Collier[1] and Thomas Mölg[1]

[1]Climate System Research Group, Institute of Geography, Friedrich-Alexander University Erlangen-Nürnberg (FAU), Erlangen, Germany

Correspondence to: Emily Collier (emily.collier@fau.de)

Abstract.

Climate impact assessments require information about climate change at regional and ideally local scales. In dendroecological studies, this information has traditionally been obtained using statistical methods, which preclude the linkage of local climate changes to large-scale drivers in a process-based way. As part of recent efforts to investigate the impact of climate change on forest ecosystems in Bavaria, Germany, within the BayTreeNet project, we developed a high-resolution atmospheric modelling dataset, BAYWRF, for the region of Bavaria over the thirty-year period of September 1987 to August 2018. The atmospheric model employed in this study, WRF, was configured with two nested domains of 7.5- and 1.5-km grid spacing, centred over Bavaria and forced at the outer lateral boundaries by ERA5 reanalysis data. Based on a shorter evaluation period of September 2017 to August 2018, we evaluate two aspects of the simulations: (i) we assess model biases compared with an extensive network of observational data at both two-hourly and daily mean temporal resolutions, and (ii) we investigate the influence of using grid analysis nudging. The model represents variability in near-surface meteorological conditions well, with a clear improvement when nudging is used, although there are cold and warm biases in winter and summer, respectively. We also present a brief overview of the full dataset, which will provide a unique and valuable tool for investigating climate change in Bavaria with high interdisciplinary relevance. Data from the finest resolution WRF domain are available for download at daily temporal resolution from a public repository at the Open Science Framework (Collier, 2020; https://www.doi.org/10.17605/OSF.IO/AQ58B).

1 Introduction

The forcing of climate change in modern times is clearly of global nature, and many important scientific problems can be understood at the global scale as well (e.g., Held and Soden, 2006). Climate impact assessments, however, must also understand the effects at regional and even local scales in order to develop appropriate adaptation and mitigation measures. Although local phenomena such as glaciers, lakes, vegetation patterns, or stream flow show a strong dependence on the large-scale climate dynamics, these proxies experience further variability when the large-scale signal is transferred to their

30 location (e.g., Mölg et al., 2014). In order to contextualize local changes, there is a need to link local climate to the large-scale climate, ideally in a process-based way.

In dendroclimatological studies, the traditional approach is to compute a calibration function between local or regional tree-ring parameters and climatic variables. Typically, such a statistical relationship would try to utilize local station data (which are generally sparse), gridded observations (which tend to be coarse resolution), or indices of large-scale climate dynamics (which describe coupled atmosphere-ocean modes) as the climatic influence (e.g., Hochreuther et al., 2016). Besides known problems like stationarity (e.g., Frías et al., 2006), statistical approaches also limit the possibilities to explain the influences at the various scales on a process-resolving level. Dynamical downscaling with a full numerical atmospheric model provides a physical answer (Giorgi and Mearns, 1991), yet the disadvantage is the high computational cost. Hence, dynamical downscaling at near-kilometer resolution has traditionally been performed on a case-study basis for weather events (e.g., Gohm et al., 2008). Multi-decadal simulations, on the other hand, were typically limited to resolutions of tens of kilometers (e.g., Di Luca et al., 2016). With the progress of computational resources, dynamical downscaling is becoming a candidate for climate impact studies that require local-scale information, and the first decadal simulations at ~1-km resolution are now available (e.g., Collier et al., 2018). From the resultant model output, impact studies could utilize information about local meteorological conditions at high-spatial and high-temporal resolution, and over long, climatologically relevant temporal periods. Moreover, the physically consistent output would enable to generate the said process understanding of influences across the various climatic scales.

The management of forests is a classical impact study where adaptation and mitigation measures meet the heterogeneous effects of climate change at local scales (e.g., Lindner et al., 2014). With this background, the project BayTreeNet was started recently under the umbrella of the interdisciplinary climatological research network Bayklif (https://www.bayklif.de; last accessed 1 March 2020), and aims to investigate the response of forest ecosystems to current and future climate dynamics across different growth areas in Bavaria, Germany. The project comprises a network of 10 measurement sites where meteorological and dendroecological data will be monitored and used both for research and for public and educational outreach. The locations were selected carefully to account for ecological and elevational variety in the study region, and the sites are currently in the process of being installed. High-temporal (approximately daily) and high-spatial resolution data is a key component of dendroecological impact studies, since the physiological behavior of trees, their structural properties and functional wood anatomy, as well as other important parameters such as wood density and mortality risk are not only influenced by seasonal averages, but also by short-term extreme events and weather anomalies (e.g., Bräuning et al., 2016).

60

Previous regional climate simulations including Bavaria over continuous multi-decadal periods were performed with model resolutions as high as 5-7 km and up to the year 2009 (e.g., Berg et al., 2013; Warscher et al., 2019). However, to the best of our knowledge, such datasets at the kilometer scale and up to the near present do not yet exist, despite previous research

highlighting the importance of convection-permitting resolution in this region (Fosser et al., 2014). We address this data gap

65 by performing simulations with an atmospheric model, configured with convection-permitting spatial resolution in a nested domain over Bavaria, for the recent climatological period of 1987 to 2018. These data were generated as part of the aforementioned BayTreeNet project in order to assess the dendroecological consequences of local climate change on forests in the study region. These data will also find multidisciplinary interest among researchers assessing ecological and human dependencies on the climate for scientific and practical questions.

70 **2 Methods**

2.1 Atmospheric model

The atmospheric simulations were performed using the advanced research version of the Weather Research & Forecasting (WRF) model v. 4.1 (Skamarock and Klemp, 2008) configured with two one-way-nested domains of 7.5- and 1.5-km grid spacing situated over Bavaria (Fig. 1), hereafter referred to as D1 and D2. Terrain data were taken from NASA Shuttle Radar

75 Topographic Mission data re-sampled to 1-km and 500-m grids (Jarvis et al., 2008; https://cgiarcsi.community/data/srtm-90m-digital-elevation-database-v4-1; last accessed 24 May 2020) for D1 and D2, respectively, while land-use data was updated based on the European Space Agency Climate Change Initiative Land Cover data at 300-m spatial resolution (http://maps.elie.ucl.ac.be/CCI/viewer/download.php; last accessed 18 April 2018). The physics and dynamics options used in the simulations are based on recent convection-permitting applications of WRF by the authors (Collier et al., 2019) and

80 are summarized in Table 1. We note that no additional urban physics were enabled beyond the default parameterization used by the Noah family of land surface models (Liu et al., 2006) and land-use sub-tiling was not enabled.

Forcing data at the lateral boundary of D1 and bottom boundaries of both domains was taken from the ERA5 reanalysis (Copernicus Climate Change Service (C3S), 2017) at three-hourly temporal resolution. The 30-year simulation was divided

85 into 30 annual simulations that were run continuously from 15 August of year $n-1$ to 31 August of year n. The first 16 days of each simulation were discarded as spin-up time, retaining data from 1 September of year $n-1$ onwards. Atmospheric carbon dioxide (CO_2) was updated in WRF for each simulation year using annually and globally averaged concentrations at the surface from the National Oceanic and Atmospheric Administration Earth System Research Laboratory (Tans and Keeling, 2019). Each simulation employed the CO_2 concentration of year n, which ranged from 351 to 407 ppm between

90 1988 and 2018. All other parameters and bottom boundary conditions (e.g., vegetation and land use) were held constant for all simulations. Therefore, they do not capture the impact of known land-use changes over the study period (e.g., Fuchs et al., 2013).

Each run required 12 days of wall-time with 320 processors on the Meggie compute cluster at the Erlangen Regional

95 Computing Center, for a total of 2.86 million core hours. The model was compiled using intel 17.0 compilers and run using

distributed-memory parallelization. Model output was written at two-hourly intervals, amounting to more than 55 TB of data, in addition to ~30 TB of pre-processing and input files.

2.2 Model Evaluation

100 For detailed model evaluation, we selected the period of 00 UTC 1 September 2017 to 00 UTC 1 September 2018, as data availability is highest closest to present day and the summer of 2018 contained a record heatwave with drought conditions (Beyer, 2018). Neither extensive physics optimization nor a longer evaluation period was possible due to the computational expense of the simulations. For the evaluation period, we compared two test simulations (see Sect. 2.3) with data from the German Weather Service (DWD) Climate Data Center for all stations in Bavaria with hourly temporal resolution available,

105 which provide good spatial coverage of our study area (Table 2; Fig. 2). We compared the following near-surface atmospheric variables: air temperature and relative humidity at 2 m (T and RH), zonal and meridional wind components at 10 m (U and V), surface pressure (PS), and precipitation (PR). In our comparison, we excluded measurement sites where the observed terrain height differed from the modelled value by more than 100 m (similar to e.g., Vionnet et al., 2019), corresponding to four sites in total for all variables except for PS (three) and PR (nine). After this exclusion, the average

110 difference between modelled and observed terrain height at all stations is within ± 8 m for each dataset. We also excluded any days with missing observational data when computing daily statistics. We did not evaluate radiation variables, as only sunshine hours are available from the DWD in sufficiently large sample sizes. However, for understanding temperature biases in WRF during summer 2018, we used incoming shortwave radiation from the DWD Climate Data Center dataset entitled "*Hourly station observations of solar incoming (total/diffuse) and longwave downward radiation for Germany*"

115 (Table 2). In total, there were four sites with both incoming shortwave (SW) and T data available in Bavaria between 1 June and 31 August 2018 whose elevation was represented within ±100 m in D2: Nürnberg (id 3668), Weihenstephan-Dürnast (5404), Würzburg (5705), and Fürstenzell (5856).

For statistical analysis, we computed the mean deviation (MD), mean absolute deviation (MAD), and the coefficient of

120 determination (R^2) between station data and data from the closest grid point in D2 without spatial interpolation at two-hourly and daily temporal frequency. The MD, also referred to here as the model bias, and the MAD were computed from observation minus model. For precipitation, only daily totals were evaluated, and the MD and MAD were computed considering only days with non-zero observed precipitation.

125 Finally, we also compared night-time land surface temperature (LST) from the MODIS MYD11A1 dataset (Table 2) at 1-km spatial and daily temporal resolution with simulated skin temperature in D2 for the period of 1 June to 31 August 2018. The night view time ranged from 1.2 to 2.8 hours in local solar time, with a domain and time averaged value of 2.2 hours. As WRF data were only available at two-hourly timesteps, we averaged 00 and 02 UTC (01 and 03 local time) data from D2 for

comparison with MODIS. In our comparison, we excluded nights when MODIS had more than 50% missing data over D2, leaving a sample size of 52.

2.3 Forcing Strategy

For the evaluation period, we compared two simulations with different forcing approaches, one excluding and one including grid analysis nudging to constrain drift in the large-scale circulation (e.g., Bowden et al., 2013). We refer to these simulations as WRF_NO_NUDGE and WRF_NUDGE in Section 3.1, respectively. For the WRF_NUDGE simulation, analysis nudging was applied in D1 outside of the planetary boundary layer and above the lowest 10 model levels using the default strength (3.0×10^{-4}) for temperature and winds and reduced strength (5.0×10^{-5}) for the water vapor mixing ratio (e.g., Otte et al., 2012), consistent with a previous decadal application of WRF (Collier et al., 2018). Given the computational expense of each annual simulation, we did not attempt to optimize the nudging coefficients for our study area and instead evaluate simply whether nudging in this form improves the simulated atmospheric variables or not.

2.4 Climatological Analysis

To briefly evaluate the full climatological simulation, we compared simulated and observed monthly mean T from the DWD dataset '*MO_TT_MN004*' (Table 2), with a sample size of 26 stations that remained after filtering for height differences exceeding 100 m, the presence of missing data, and stations located in grid cells classified as urban (see Sect. 3.1). For the distributed trend analysis, we did not apply a field significance test (e.g., Wilks, 2016) due to the small sample size. Future users should rigorously evaluate biases for the variables, time periods, and resolutions relevant to their particular applications.

We note that unphysically large sub-surface temperatures were simulated at a number of glacierized grid points, primarily during the months of July to September. Considering all of D2, the daily average number of affected grid cells was 24, compared with 294 glacierized and 122,500 total cells. The maximum number of affected grid points was 274 on 31 August 2017, corresponding to 0.2% of D2. In addition, over the climatological simulation, only one grid point in Bavaria was affected (J = 71, I = 285; 47.4952°N, 13.6039°E). Surface temperature remained physical, since it is limited at the melting point over glacier surfaces, and soil moisture was unaffected, since it is specified to be fully saturated in glacierized grid cells. No other land-use categories were affected, and adjacent grid points were also unaffected, as the land surface model operates as a column model with no lateral communication. To preclude usage of these data, sub-surface temperature was set to missing where it exceeded 273.16 at glacierized grid points in BAYWRF. More information about this numerical issue is available on the model's GitHub repository (https://github.com/wrf-model/WRF/issues/1185; last accessed 24 May 2020).

3 Results & Discussion

3.1 Model Evaluation

160   Averaged over the evaluation year, both WRF simulations capture the magnitude and variability of sub-diurnal near-surface meteorological conditions at most sites well (Fig. 3; Table 3). The interquartile range (IQR; range between upper and lower quartile) of MDs is one order of magnitude smaller than the observed standard deviation for all variables. As expected, variability is best captured for *T* and *PS*, with R^2 values that uniformly exceed 0.87 and 0.96, respectively. Those of *RH* have a larger range but a lower quartile above ~0.55. Compared with these variables, the model shows less skill in simulating sub-diurnal variability in winds, with lower quartiles of R^2 for *U* and *V* of approximately 0.39 and 0.27, respectively. Shifting to daily timescales, both simulations represent variability in daily total *PR* surprisingly well, with IQRs of MDs below ~1.25 mm and lower quartiles of R^2 exceeding 0.18 and 0.33, depending on the simulation. Previous studies have reported Root Mean Square Deviations (RMSD). For direct comparison, the mean RMSD in WRF_NUDGE for two-hourly *T* and *RH* is 2.67 K and 13.7%, respectively, and for daily total precipitation is 5.27 mm. These values are similar to but lower than previously reported biases in WRF at 5-km grid spacing over Bavaria for the period of 2001—2009 (Warscher et al., 2019).

Examination of model biases on a monthly basis reveals further insights into the model performance (Fig. 4). The amplitude of the annual cycle is overpredicted in WRF, indicating that the good average agreement in *T* results from compensating biases: there is a cold bias in WRF in winter, a well-known issue with the model over snow-covered surfaces (e.g., Tomasi et al., 2017), and a warm bias in summer (Fig. 4a). The latter bias results in an underprediction of *RH* during this season (Fig. 4b), suggesting that WRF represents absolute humidity more accurately. The summer temperature bias is also more sustained than the winter one, resulting in the long tails (heads) in the distribution of MDs of *T* (*RH*) in Fig. 3. There is also a general underprediction of near-surface winds from fall to early winter, as exemplified by the results for *U* in Fig. 4c and the slight positive skewness of the distribution of MDs for both *U* and *V* in Fig. 3, consistent with overly stable atmospheric conditions resulting from the cold bias. Finally, the model tends to overestimate precipitation in early spring and underestimate it in summer and fall.

Figure 5 shows a representative timeseries of *T* and *SW* for the station in Nürnberg (3668) in June 2018. The timeseries illustrates that the positive temperature bias in summer 2018 results from two distinct contributions. First, there is an overestimation of daytime maximum *T*, coinciding with an overestimation of *SW*. This relationship is observed both at Nürnberg and at the other three stations for which both datasets are available (Fig. 6a; cf. Sect. 2.2). The overestimation suggests there is an underestimation of either daytime cloudiness or its impact on incoming *SW* at the surface, likely stemming from the microphysics parameterization. Second, there is an overestimation of night-time minimum *T*, suggesting that land-surface processes may play a role. Of the 101 stations with *T* measurements available, the dominant land-use categories of the grid cells containing stations are: *'Urban'* (10 sites); *'Dryland Cropland and Pasture'* (4 sites); *'Grassland'*

(72 sites); *'Deciduous Broadleaf Forest'* (1 sites); *'Evergreen Needleleaf Forest'* (11 sites); and, *'Mixed Forest'* (3 sites). The overestimation of night-time T is greatest at stations located in grid cells classified as urban (Fig. 6b), consistent with a previous evaluation of WRF with the Noah-MP LSM for urban and rural stations in summer (Salamanca et al., 2018). The bias amplification in urban grid cells may reflect an incorrect classification of the underlying land surface in WRF, as only the München-Stadt station (id 3379) is listed as an urban station on the DWD's list for computing heat island effects. It may also result from an overestimation of heat storage when a mosaic approach is not used, and therefore the entire grid cell is treated as urban (Daniel Fenner, personal communication). The potential role of the land-surface specification or properties is reinforced by the comparison with MODIS data (Fig. 7), which shows the largest warm biases over grid cells classified as urban or croplands while biases are smaller in forested areas. There is also a cold bias along the foothills and at higher elevations in the Alps. The biases are slightly smaller in WRF_NUDGE than in WRF_NO_NUDGE, consistent with the station-based assessment.

In addition to factors internal to WRF, we note that the driving reanalysis data may also contribute to the warm bias, at least at some locations. From the available observations, 60 stations have both valid T data between June and August 2018 and a modelled elevation in ERA5 that is within ±100 m of reality. Averaged over the summer months and all stations, ERA5 has a mean warm bias of 0.37°C. At 25 of the sites, a warm bias exceeding 0.5°C is present, with an average value over these sites of 0.92°C.

3.2 Impact of Grid Analysis Nudging

The inclusion of grid analysis nudging leads to a small but nearly uniform improvement in agreement between observed and simulated variables. The distribution of MDs is closer to zero for all variables except U and PS, while those of MADs are closer for all variables (cf. Fig. 3 and Table 3). R^2 values are also uniformly higher when nudging is used, and the lowest lower-quartile value is 0.3 in WRF_NUDGE compared with only 0.18 in WRF_NO_NUDGE. Nudging produces a particularly noticeable improvement in simulated precipitation, halving the MD and nearly doubling the R^2 values (cf. Fig. 3, Fig. 4 and Table 3). Its usage also reduces the magnitude of the seasonal temperature biases and the number of extreme occurrences of the warm bias in summer (cf. Fig. 4 and Fig. 6). Considering daily timescales (the temporal resolution of data available in BAYWRF), the agreement of WRF_NUDGE with the observations is similar or even improved (Table 4): the mean MD is largely unaffected, but the average MAD decreases and average R^2 increases. Based on these improvements, grid analysis nudging was adopted for the climatological simulations.

3.3 Climatological Simulations

Figure 8a compares simulated and observed annual mean T between 1988 and 2018 at the 33 stations with data available after filtering (cf. Sect. 2.4). WRF captures the variability in annual T well, although the data and its spread are slightly underestimated during the late 1990s and 2000s. The observations have a statistically significant trend of 0.28 K/decade (p =

0.04) while the model data do not (0.2 K/decade, p = 0.2) although this statistical analysis is very sensitive with such a small sample size. However, inspection of *T* trends by month reveals that WRF overestimates the slight cooling trends observed
225   between January and March (statistically insignificant in both data sources; not shown), due to the winter cold bias and/or potential errors in snow depth and extent, which may contribute to an underestimate of the annual warming trend. Trends are otherwise well captured, including the three months with statistically significant observed trends: April (OBS: 0.83; WRF:0.75 K/decade); June (OBS: 0.75; WRF:0.71 K/decade); and, November (OBS: 0.72; WRF: 0.71 K/decade). WRF similarly captures the variability of summer mean (June, July, August; JJA) temperature (Fig. 8b), although the warm bias at
230   the station locations is again apparent. The observed trend is 0.49 K/decade compared with 0.48 in WRF (p<0.05). Furthermore, the model captures recent extreme summers in Western and Central Europe in 2003, 2015 and 2018, which in combination with drought have had severe impacts on economies, public health (e.g., Muthers et al., 2017), and primary productivity (e.g., Ciais et al., 2005).

235   Here we note that in addition to the potential factors contributing to temperature biases discussed in Section 3.1, evaluation of the climatological simulation is also affected by discontinuities in station location. One example is Nürnberg (id 3668), which moved on 4 December 1995 from (49.4947ºN, 11.0806ºE) to (49.5030ºN, 11.0549ºE). The older station position is shifted one grid cell to the south and one grid cell to the west compared with its current location, corresponding to a shift in land use from urban (old position) to grasslands (new). Any discontinuities in location and underlying surface type are not
240   captured since the most recent station positions are used for extracting *T* data from D2.

Spatially distributed trends in *T* are strongest and significant over the largest in area during JJA (Fig. 9a; other seasons not shown), ranging from ~0.3 to 0.7 K/decade over Bavaria. Trends in precipitable water are likewise uniformly positive over the study region, ranging from ~0.2 to 0.3 mm/decade. The trends of both fields also have a positive gradient between
245   southwestern and northeastern Bavaria. These results agree qualitatively and quantitively with previous studies (e.g., Alshawaf et al., 2017).

4 Data Availability

Data from BAYWRF are available for download on the Open Science Framework (OSF; Collier, 2020; https://www.doi.org/10.17605/OSF.IO/AQ58B). Due to the size of the simulations, we have only provided daily mean data
250   from the finest WRF domain (D2; 1.5-km grid spacing) after cropping close to the extent of Bavaria and removing vertical levels above ~ 200 hPa, amounting to 450 GB in total. Data are divided into three- and four-dimensional fields by year and month, with respective file sizes of ~150 MB and 1.1 GB. For the four-dimensional data, perturbation and base-state atmospheric pressure (WRF variables P and PB) and geopotential (PH and PHB) were combined to generate full model

fields, while perturbation potential temperature (T) was converted to atmospheric temperature. Subsets of D1 or sub-diurnal
255   data can be made available upon request.

5 Conclusions

We presented a climatological, convection-permitting simulation with the atmospheric model WRF over Bavaria for the
period of September 1987 to August 2018. For the evaluation period of September 2017 to August 2018, we compared the
simulations with meteorological measurements across Bavaria and evaluated the impact of using grid-analysis nudging. We
260   found that the model reproduced variability in near-surface meteorological conditions well, although seasonal temperature
biases were present. Grid analysis nudging decreased the mean deviations and increased the correlations between simulations
and observations at the majority of sites for nearly all evaluated atmospheric variables, with a particularly noticeable
improvement for simulated daily precipitation. BAYWRF provides a useful database for linking large-scale climate, as
represented by the ERA5 reanalysis, to mesoscale climate over Germany, to local conditions in Bavaria, in a physically
265   based way. The data are intended for dendroecological research applications but would also provide a valuable tool for
investigations of the climate dependence of economic, societal, ecological, and agricultural processes in Bavaria.

6 Author contributions

EC performed the simulations, analyzed the data and wrote the manuscript. TM developed the study concept and wrote the
manuscript.

270   ## 7 Competing interests

The authors declare that they have no conflict of interest.

8 Acknowledgements

This project is sponsored by the Bavarian State Ministry of Science and the Arts in the context of the Bavarian Climate
Research Network (bayklif). We gratefully acknowledge the compute resources and support provided by the Erlangen
275   Regional Computing Center (RRZE) and we thank Thomas Zeiser for his assistance with the timely completion of the
simulations.

References

Alshawaf, F., Balidakis, K., Dick, G., Heise, S. and Wickert, J.: Estimating trends in atmospheric water vapor and

temperature time series over Germany, Atmos. Meas. Tech., doi:10.5194/amt-10-3117-2017, 2017.

280 Berg, P., Wagner, S., Kunstmann, H. and Schädler, G.: High resolution regional climate model simulations for Germany: Part I-validation, Clim. Dyn., doi:10.1007/s00382-012-1508-8, 2013.

Beyer, M.: Hitzewelle Sommer 2018 - Einordnung und Ausblick, [online] Available from: https://www.dwd.de/DE/wetter/thema_des_tages/2018/8/6.html (Accessed 1 August 2019), 2018.

Bowden, J. H., Nolte, C. G. and Otte, T. L.: Simulating the impact of the large-scale circulation on the 2-m temperature and

285 precipitation climatology, Clim. Dyn. [online] Available from: http://link.springer.com/article/10.1007/s00382-012-1440-y, 2013.

Bräuning, A., De Ridder, M., Zafirov, N., García-González, I., Dimitrov, D. P. and Gärtner, H.: TREE-RING FEATURES: INDICATORS of EXTREME EVENT IMPACTS, IAWA J., doi:10.1163/22941932-20160131, 2016.

Ciais, P., Reichstein, M., Viovy, N., Granier, A., Ogée, J., Allard, V., Aubinet, M., Buchmann, N., Bernhofer, C., Carrara,

290 A., Chevallier, F., De Noblet, N., Friend, A. D., Friedlingstein, P., Grünwald, T., Heinesch, B., Keronen, P., Knohl, A., Krinner, G., Loustau, D., Manca, G., Matteucci, G., Miglietta, F., Ourcival, J. M., Papale, D., Pilegaard, K., Rambal, S., Seufert, G., Soussana, J. F., Sanz, M. J., Schulze, E. D., Vesala, T. and Valentini, R.: Europe-wide reduction in primary productivity caused by the heat and drought in 2003, Nature, doi:10.1038/nature03972, 2005.

Collier, E.: BAYWRF, [online] Available from: https://www.doi.org/10.17605/OSF.IO/AQ58B, 2020.

295 Collier, E., Mölg, T. and Sauter, T.: Recent atmospheric variability at Kibo summit, Kilimanjaro, and its relation to climate mode activity, J. Clim., 31(10), 3875–3891, doi:10.1175/JCLI-D-17-0551.1, 2018.

Collier, E., Sauter, T., Mölg, T. and Hardy, D.: The influence of tropical cyclones on circulation, moisture transport, and snow accumulation at Kilimanjaro during the 2006 - 2007 season, J. Geophys. Res. Atmos., 2019.

Copernicus Climate Change Service (C3S): ERA5: Fifth generation of ECMWF atmospheric reanalyses of the global

300 climate., Copernicus Clim. Chang. Serv. Clim. Data Store [online] Available from: https://cds.climate.copernicus.eu/cdsapp#!/home (Accessed 16 June 2019), 2017.

Esty, W. W. and Banfield, J. D.: The Box-Percentile Plot, J. Stat. Softw., doi:10.18637/jss.v008.i17, 2003.

Fosser, G., Khodayar, S. and Berg, P.: Benefit of convection permitting climate model simulations in the representation of convective precipitation, Clim. Dyn., doi:10.1007/s00382-014-2242-1, 2014.

305 Frías, M. D., Zorita, E., Fernández, J. and Rodríguez-Puebla, C.: Testing statistical downscaling methods in simulated climates, Geophys. Res. Lett., doi:10.1029/2006GL027453, 2006.

Fuchs, R., Herold, M., Verburg, P. H. and Clevers, J. G. P. W.: A high-resolution and harmonized model approach for reconstructing and analysing historic land changes in Europe, Biogeosciences, doi:10.5194/bg-10-1543-2013, 2013.

Giorgi, F. and Mearns, L. O.: Approaches to the simulation of regional climate change: A review, Rev. Geophys.,

310 doi:10.1029/90RG02636, 1991.

Gohm, A., Mayr, G. J., Fix, A. and Giez, A.: On the onset of bora and the formation of rotors and jumps near a mountain gap, Q. J. R. Meteorol. Soc., doi:10.1002/qj.206, 2008.

Held, I. M. and Soden, B. J.: Robust responses of the hydrological cycle to global warming, J. Clim., doi:10.1175/JCLI3990.1, 2006.

315 Hochreuther, P., Wernicke, J., Grießinger, J., Mölg, T., Zhu, H., Wang, L. and Bräuning, A.: Influence of the Indian Ocean Dipole on tree-ring δ18O of monsoonal Southeast Tibet, Clim. Change, doi:10.1007/s10584-016-1663-8, 2016.

Hong, S. Y., Noh, Y. and Dudhia, J.: A new vertical diffusion package with an explicit treatment of entrainment processes, Mon. Weather Rev. [online] Available from: http://journals.ametsoc.org/doi/abs/10.1175/MWR3199.1, 2006.

Iacono, M. J., Delamere, J. S., Mlawer, E. J., Shephard, M. W., Clough, S. A. and Collins, W. D.: Radiative forcing by long-lived greenhouse gases: Calculations with the AER radiative transfer models, J. Geophys. Res., 113(D13), D13103, doi:10.1029/2008JD009944, 2008.

Jarvis, A., Reuter, H. I., Nelson, A. and Guevara, E.: Hole-filled SRTM for the globe Version 4, available from CGIAR-CSI SRTM 90m Database (http//srtm. csi. cgiar. org), 2008.

Jiménez, P. A., Dudhia, J., González-Rouco, J. F., Navarro, J., Montávez, J. P. and García-Bustamante, E.: A Revised Scheme for the WRF Surface Layer Formulation, Mon. Weather Rev., 140(3), 898–918 [online] Available from: http://journals.ametsoc.org/doi/abs/10.1175/MWR-D-11-00056.1, 2012.

Kain, J. S.: The Kain–Fritsch Convective Parameterization: An Update, J. Appl. Meteorol., 43(1), 170–181, 2004.

Lindner, M., Fitzgerald, J. B., Zimmermann, N. E., Reyer, C., Delzon, S., van der Maaten, E., Schelhaas, M. J., Lasch, P., Eggers, J., van der Maaten-Theunissen, M., Suckow, F., Psomas, A., Poulter, B. and Hanewinkel, M.: Climate change and European forests: What do we know, what are the uncertainties, and what are the implications for forest management?, J. Environ. Manage., doi:10.1016/j.jenvman.2014.07.030, 2014.

Liu, Y., Chen, F., Warner, T. and Basara, J.: Verification of a mesoscale data-assimilation and forecasting system for the Oklahoma City area during the joint urban 2003 field project, J. Appl. Meteorol. Climatol., doi:10.1175/JAM2383.1, 2006.

Di Luca, A., Argüeso, D., Evans, J. P., De Elía, R. and Laprise, R.: Quantifying the overall added value of dynamical downscaling and the contribution from different spatial scales, J. Geophys. Res., doi:10.1002/2015JD024009, 2016.

Mölg, T., Maussion, F. and Scherer, D.: Mid-latitude westerlies as a driver of glacier variability in monsoonal High Asia, Nat. Clim. Chang. [online] Available from: http://www.nature.com/nclimate/journal/v4/n1/full/nclimate2055.html, 2014.

Morrison, H., Thompson, G. and Tatarskii, V.: Impact of Cloud Microphysics on the Development of Trailing Stratiform Precipitation in a Simulated Squall Line: Comparison of One- and Two-Moment Schemes, Mon. Weather Rev., 137(3), 991–1007, doi:10.1175/2008MWR2556.1, 2009.

Muthers, S., Laschewski, G. and Matzarakis, A.: The summers 2003 and 2015 in South-West Germany: Heat waves and heat-related mortality in the context of climate change, Atmosphere (Basel)., doi:10.3390/atmos8110224, 2017.

Niu, G.-Y., Yang, Z.-L., Mitchell, K. E., Chen, F., Ek, M. B., Barlage, M., Kumar, A., Manning, K., Niyogi, D., Rosero, E., Tewari, M. and Xia, Y.: The community Noah land surface model with multiparameterization options (Noah-MP): 1. Model description and evaluation with local-scale measurements, J. Geophys. Res., 116(D12) [online] Available from: http://www.agu.org/pubs/crossref/2011/2010JD015139.shtml, 2011.

er338777, 2018.
rock, W. C. and Klemp, J. B.: ScienceDirect - Journal of Computational Physics : A time-split nonhydrostatic atmospheric model for weather research and forecasting applications, J. Comput. Phys., 227, 3465–3485, 2008.

Tans, P. and Keeling, R.: Trends in Atmospheric Carbon Dioxide, [online] Available from: https://www.esrl.noaa.gov/gmd/ccgg/trends/data.html (Accessed 1 August 2019), 2019.

Tomasi, E., Giovannini, L., Zardi, D. and de Franceschi, M.: Optimization of Noah and Noah_MP WRF land surface schemes in snow-melting conditions over complex terrain, Mon. Weather Rev., doi:10.1175/MWR-D-16-0408.1, 2017.

Vionnet, V., Six, D., Auger, L., Dumont, M., Lafaysse, M., Quéno, L., Réveillet, M., Dombrowski-Etchevers, I., Thibert, E. and Vincent, C.: Sub-kilometer Precipitation Datasets for Snowpack and Glacier Modeling in Alpine Terrain, Front. Earth Sci., doi:10.3389/feart.2019.00182, 2019.

Warscher, M., Wagner, S., Marke, T., Laux, P., Smiatek, G., Strasser, U. and Kunstmann, H.: A 5 km Resolution Regional Climate Simulation for Central Europe: Performance in High Mountain Areas and Seasonal, Regional and Elevation-Dependent Variations, Atmosphere (Basel)., 10(11), 682, 2019.
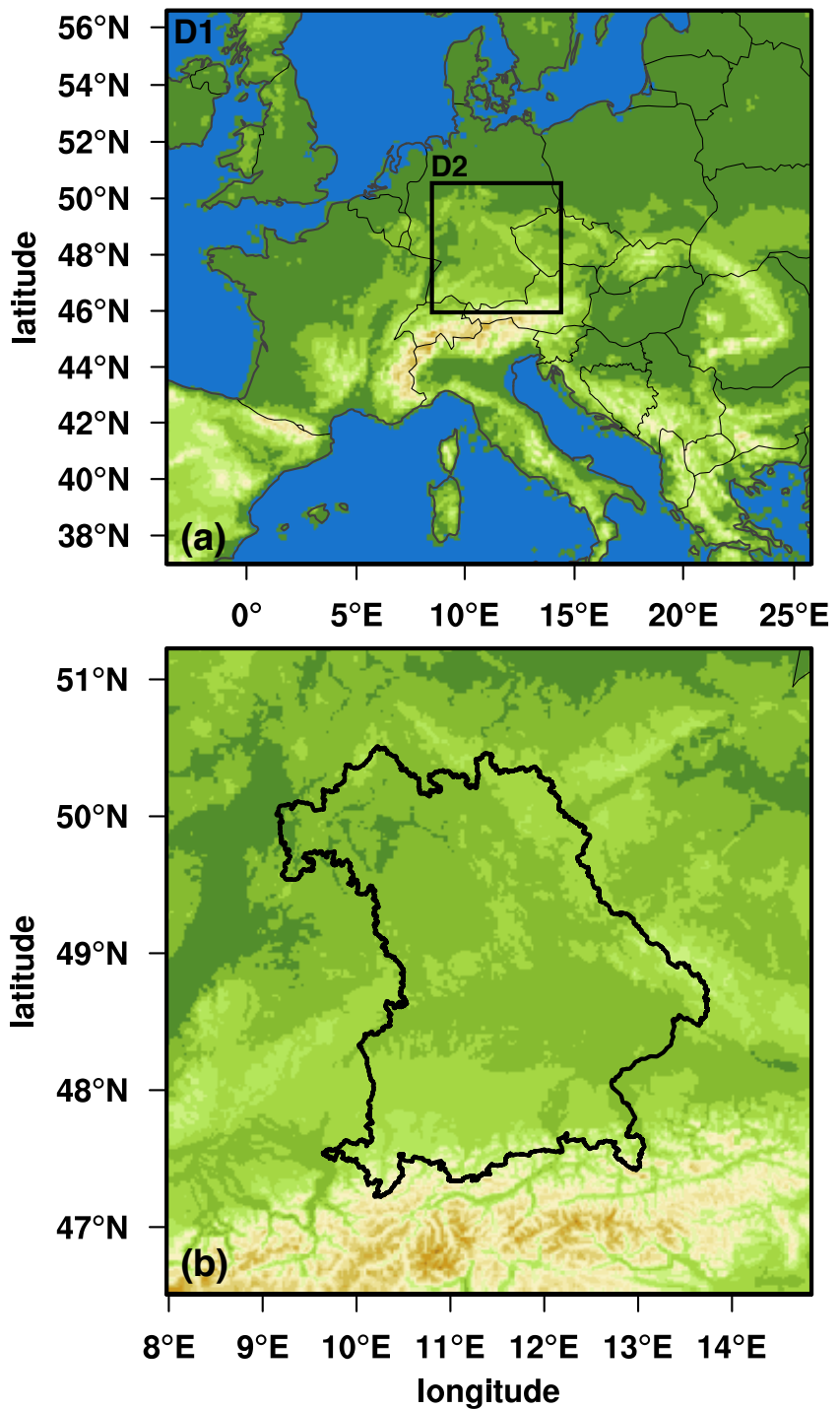
365

Figure 1: Extent and modelled topographic height [m] in WRF D1 (a) and D2 (b). The extent of D2 and of Bavaria are delineated in black in the top and bottom panels, respectively.
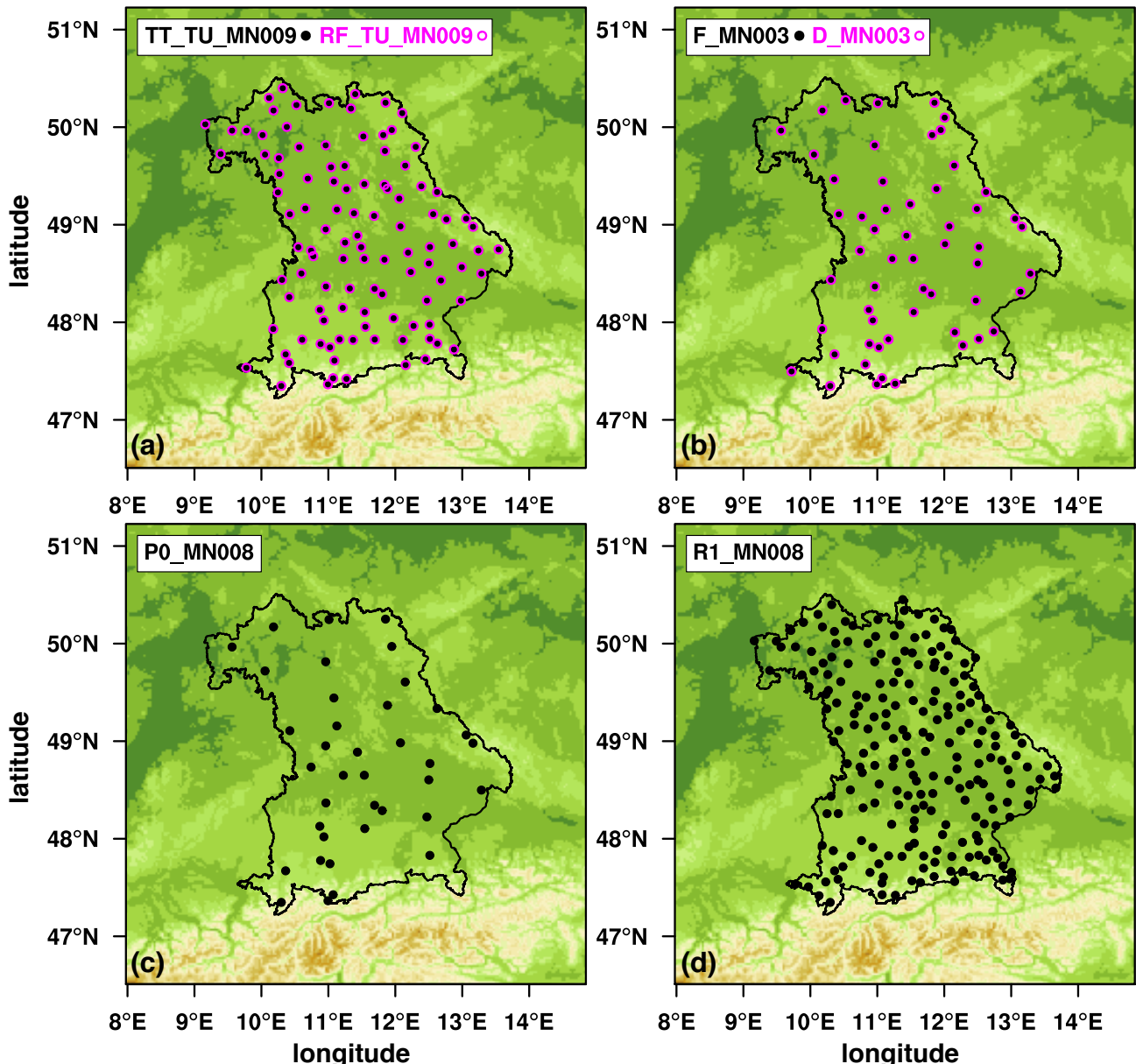
370

Figure 2: The location of the stations used for model evaluation for each dataset listed in Table 2. Datasets labelled in black are shown by filled black circles, while datasets labelled in pink are shown by open pink circles, illustrating that locations for measurements of air temperature and humidity (a; TT_TU_MN009 & RF_TU_MN009) and of wind speed and direction (b; F_MN003 & D_MN003) were the same. The locations for measurements of surface pressure (P0_MN008) and of

375 precipitation (R1_MN008) are shown in panels c and d, respectively.
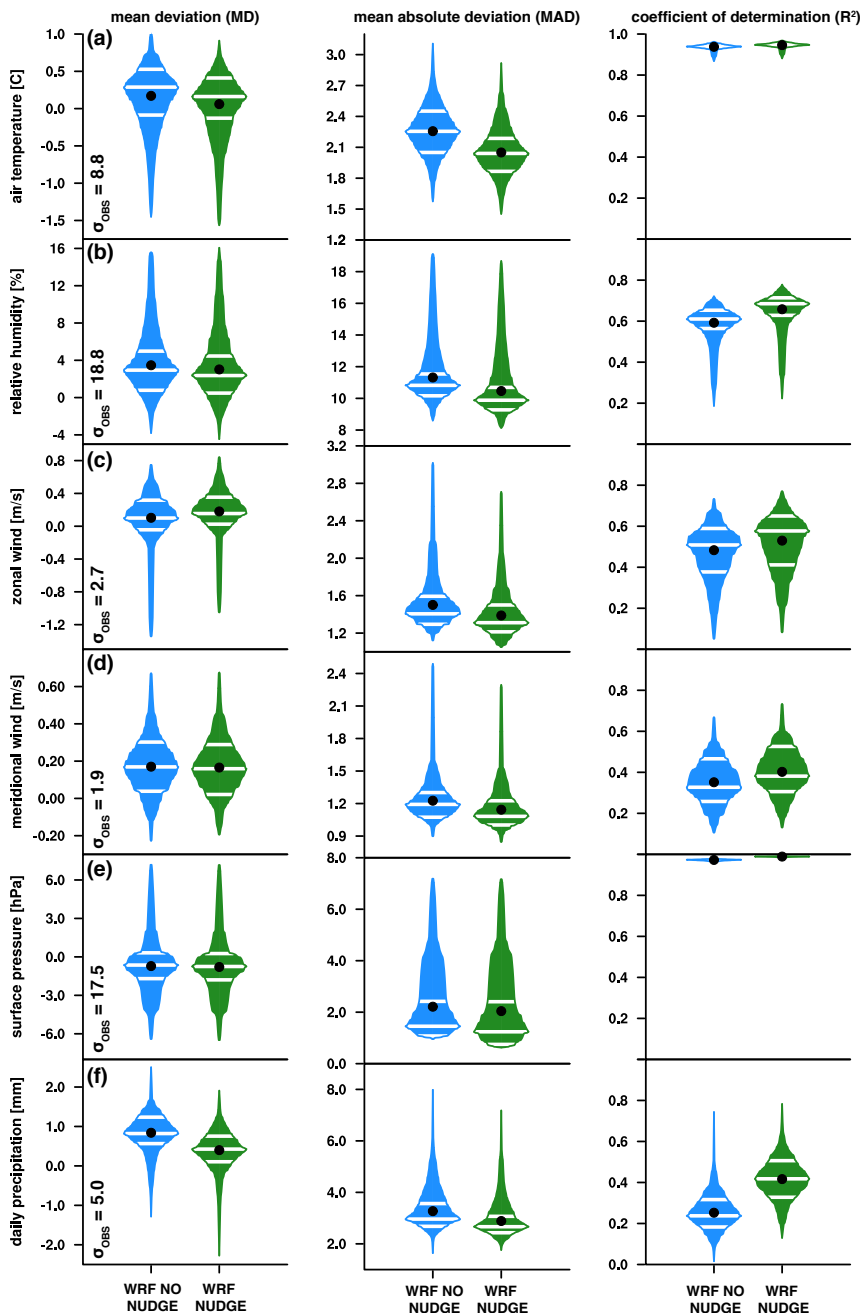
Figure 3: Box-percentile plots (Esty and Banfield, 2003) of mean deviation (MD), mean absolute deviation (MAD), and coefficient of determination (R^2) between observations and the two WRF simulations, WRF_NO_NUDGE (blue) and WRF_NUDGE (green), for 2-m (a) air temperature and (b) relative humidity, 10-m (c) zonal and (d) meridional winds, (e) surface pressure and (f) precipitation. The statistics for all variables except for precipitation were computed from two-hourly instantaneous values, while those for precipitation were computed using daily totals. The shape of the plots shows the distribution of data over their range of values, white lines delineate 25th, 50th and 75th percentiles, and a black dot indicates the mean. The observed standard deviation (σ_{obs}) for each variable is provided in the left column.
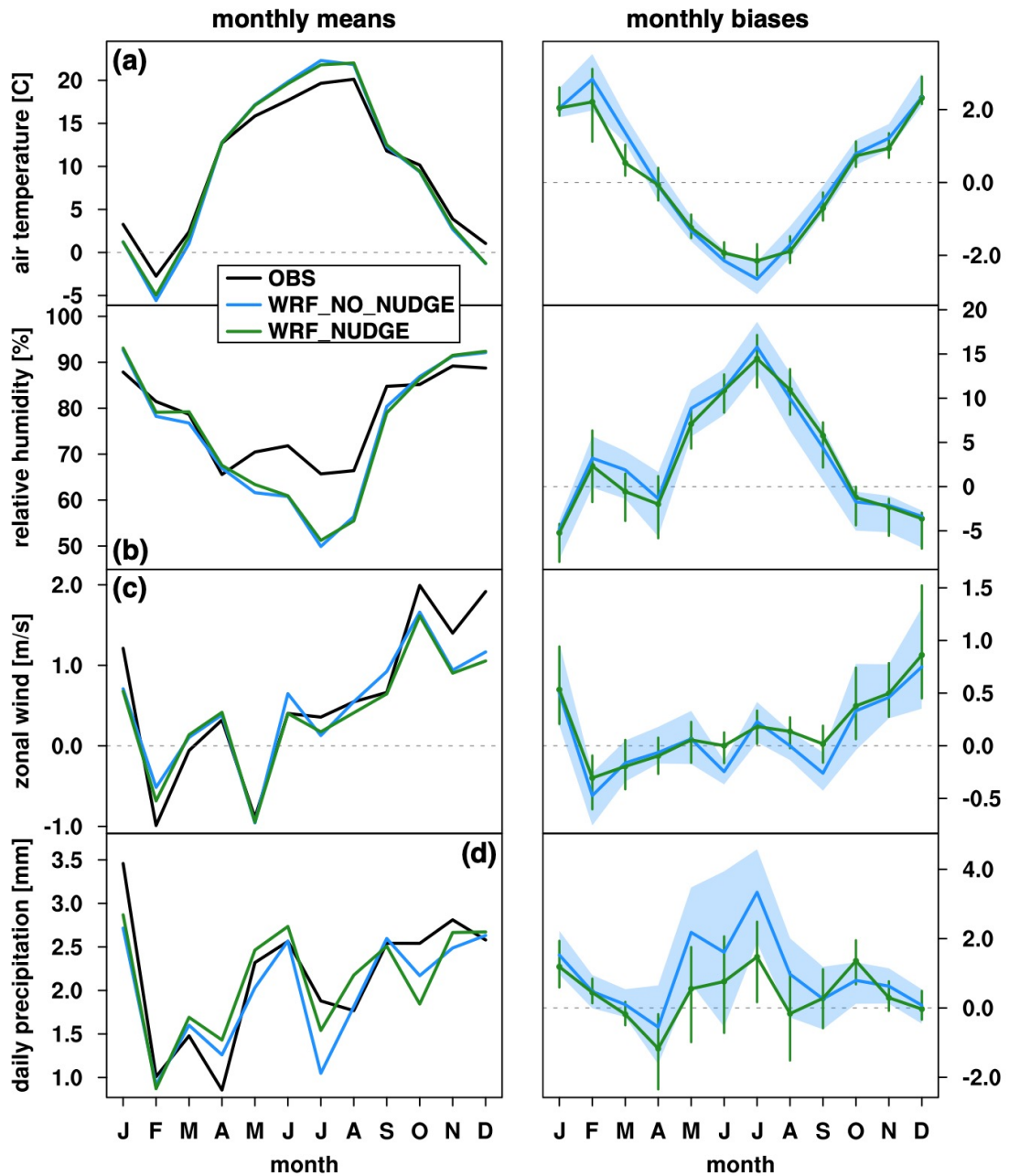
Figure 4: Timeseries of monthly mean 2-m (a) air temperature and (b) relative humidity, (c) 10-m zonal winds, and (d) daily total precipitation (left column) between September 2017 and August 2018. Observational, WRF_NO_NUDGE and WRF_NUDGE data are shown in black, blue and green, respectively. Timeseries of monthly mean biases of the same variables (right column). The mean bias over all stations is shown for each simulation using the same colour assignment, while the lower and upper quartile of the station biases is shown as a blue polygon and green bars for WRF_NO_NUDGE and WRF_NUDGE data, respectively.

395

400
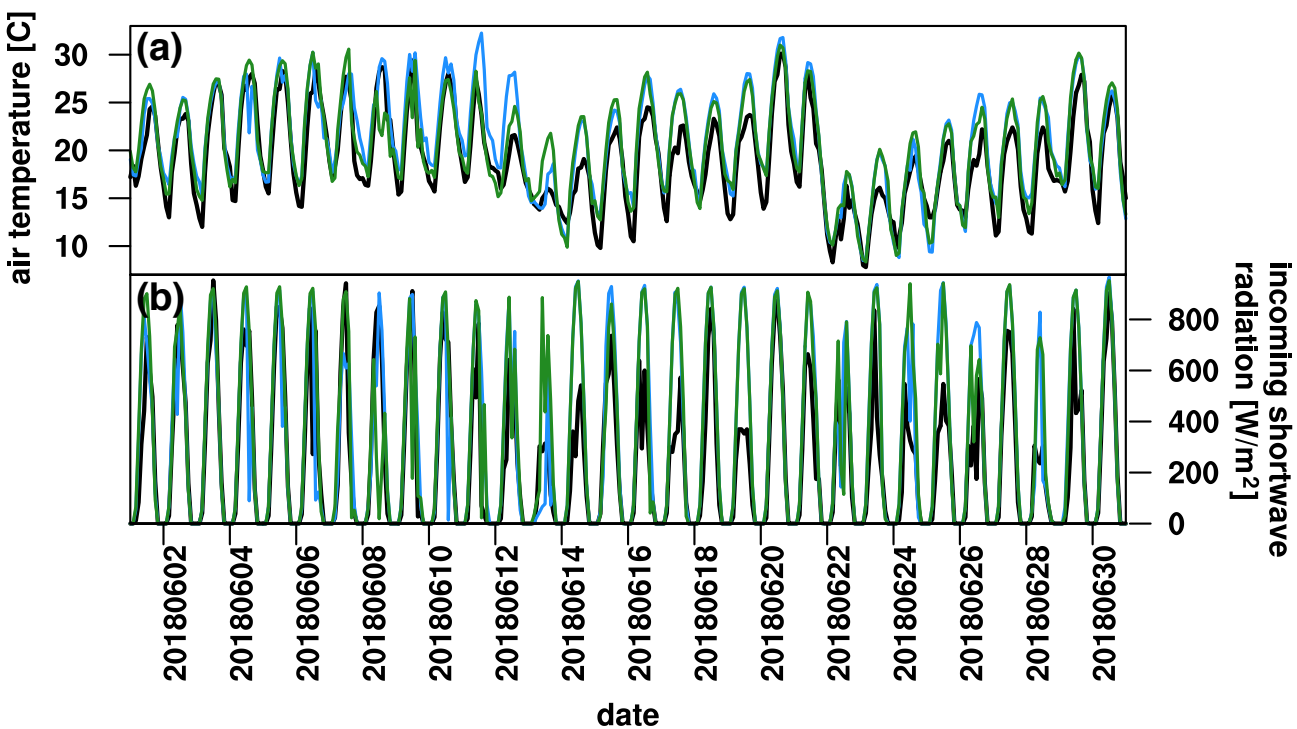
Figure 5: Timeseries of (a) 2-m air temperature and (b) incoming shortwave radiation at the station in Nürnberg (id 3668) from 1 June to 1 July 2018. Observational, WRF_NO_NUDGE and WRF_NUDGE data are shown in black, blue and green, respectively.

405
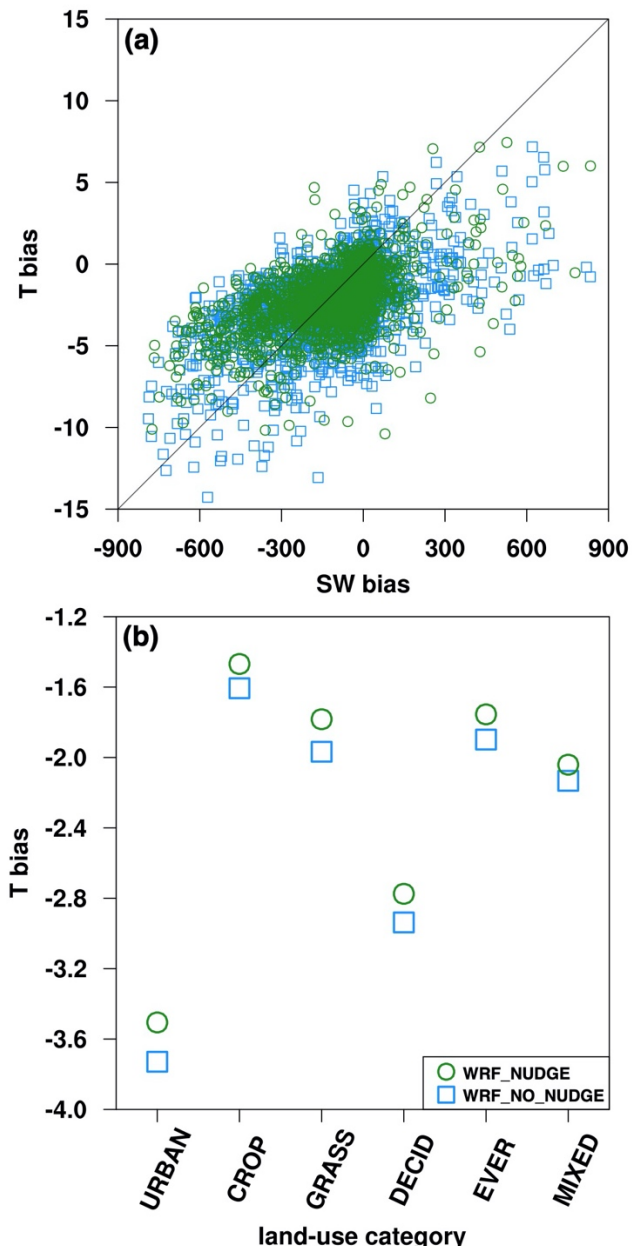
Figure 6: Scatter plots of (a) air temperature bias [ºC] vs. incoming shortwave radiation bias [W m⁻²] and (b) air temperature bias [ºC] vs. land-use category in closest grid cell to station. The category abbreviations from left to right describe: 'Urban and Built-Up Land' (10 sites); 'Dryland Cropland and Pasture' (4 sites); 'Grassland' (72 sites); 'Deciduous Broadleaf Forest' (1 sites); 'Evergreen Needleleaf Forest' (11 sites); and, 'Mixed Forest' (3 sites). For both panels, data from WRF_NO_NUDGE and WRF_NUDGE are displayed as blue square and green circle markers, respectively.

410

415

420
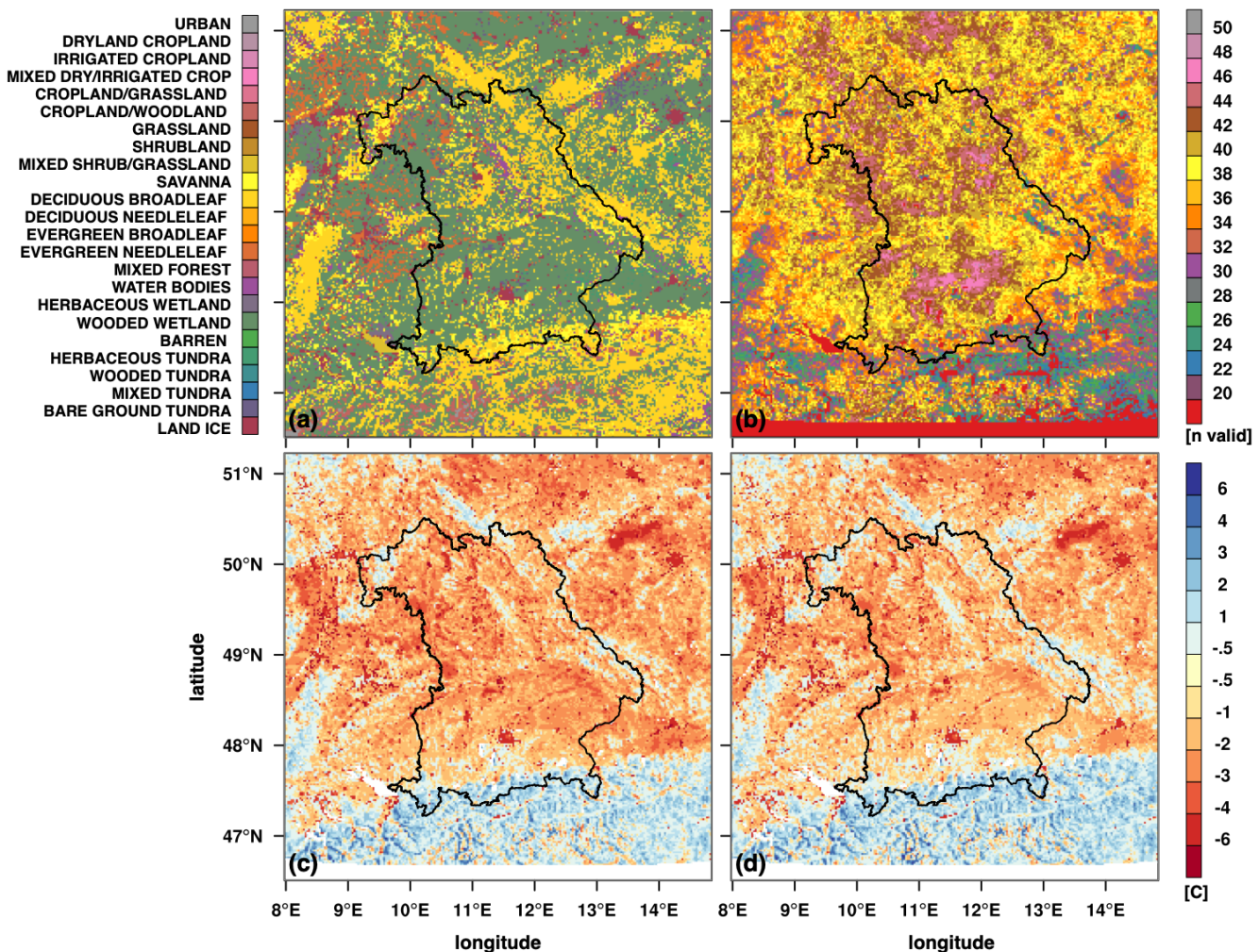
Figure 7: (a) Land-use classification in D2. (b) Number of timesteps with valid night-time LST data in the MODIS MYD11A1 dataset between 1 June and 31 August 2018 out of a maximum of 52 with less than 50% missing data in D2. The average difference in observed and simulated LST for (c) WRF_NO_NUDGE and (d) WRF_NUDGE.

430

435
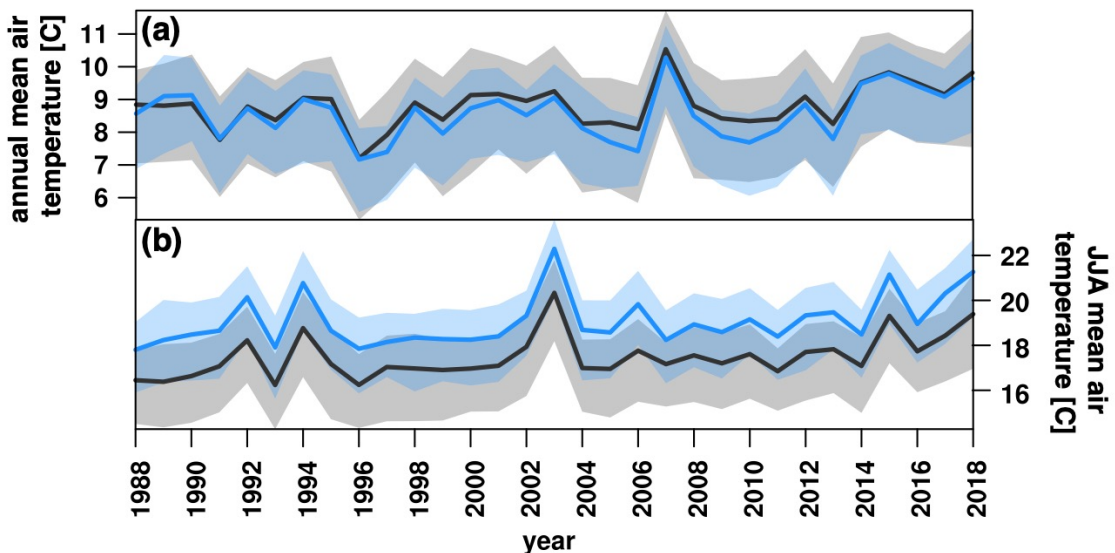
Figure 8: Comparison of (a) annual mean and (b) JJA mean 2-m air temperature from 1988 to 2018 averaged over all observations (black curve) and the corresponding grid points in WRF (blue curve). The shaded polygons delineate the range of values. To maximize data availability, annual means were computed from September of year *n-1* to August of year *n*.

440

445

450
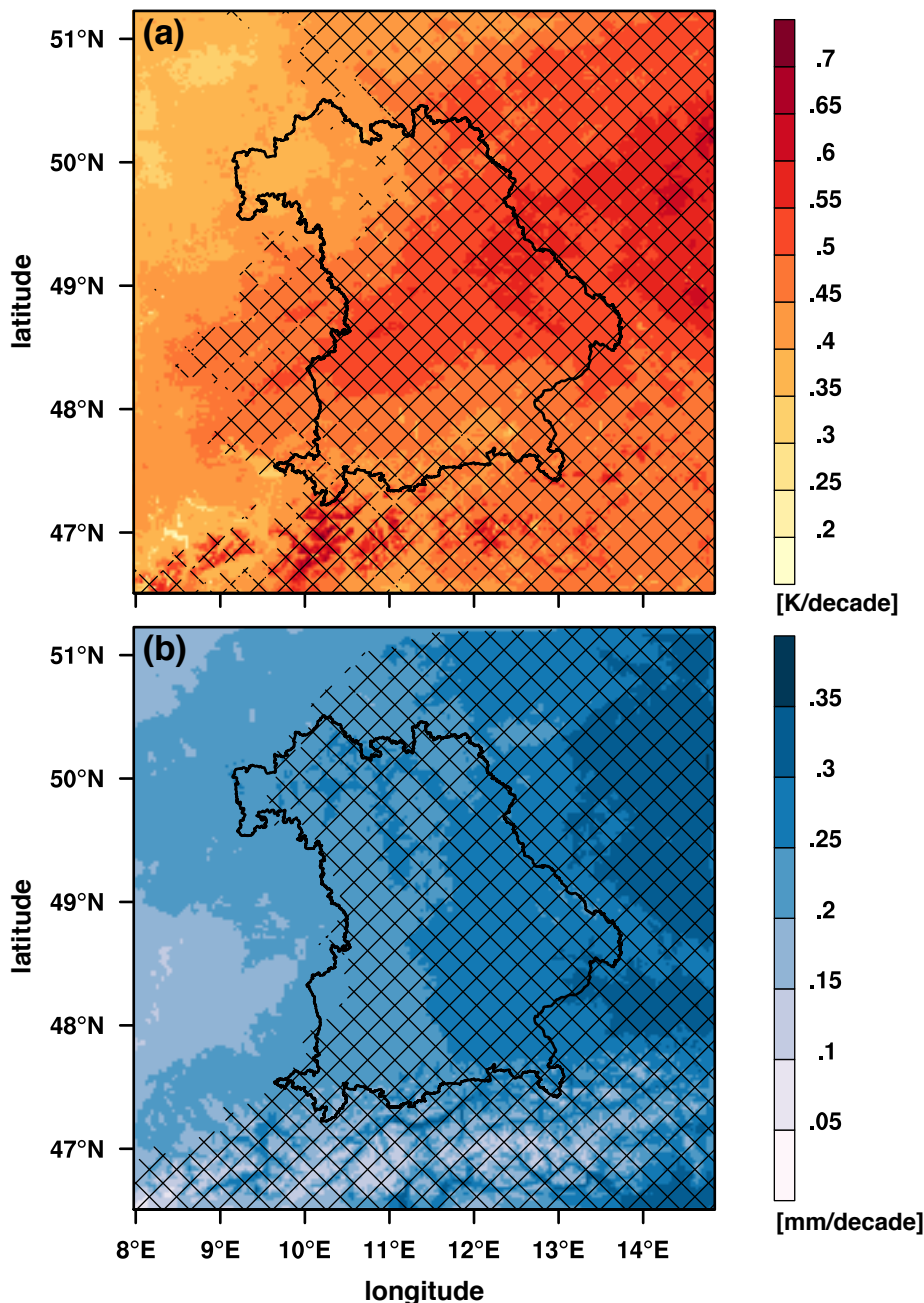
Figure 9: Spatially distributed trends of (a) JJA mean 2-m air temperature and (b) annual mean precipitable water over the climatological simulation period. Cross hatching shows where the trend is significant at the 95% level.

455

Table 1: A summary of the WRF configuration used for the simulations.

Table 1: WRF configuration		
Domain configuration		
Horizontal grid spacing	7.5 & 1.5 km (D1–2)	
Grid dimensions	351x301, 351x351	
Time step	45 & 9 s	
Vertical levels	60	
Model top pressure	1000 hPa	
Model physics		
Radiation	RRTMG	(Iacono et al., 2008)
Microphysics	Morrison	(Morrison et al., 2009)
Cumulus	Kain-Fritsch (none in D2)	(Kain, 2004)
Planetary boundary layer	Yonsei State University	(Hong et al., 2006)
Atmospheric surface layer	Monin Obukhov	(Jiménez et al., 2012)
Land surface	Noah-MP	(Niu et al., 2011)
Dynamics		
Top boundary condition	Rayleigh damping	
Diffusion	Calculated in physical space	

460

Table 2: A summary of data used for model evaluation. Rows highlighted in grey provide information about observational data from the DWD CDC Data Portal, whose measurement locations are shown in Figure 2.

Dataset Name	Variable [unit]	Temporal Resolution	Total Stations in Bavaria	Version	Access URL	Last Accessed	Dataset Description
TT_TU_MN009	2-m air temperature [°C]	Hourly	106	v19.3	https://cdc.dwd.de/portal		https://cdc.dwd.de/sdi/pid/TT_TU_MN009/DESCRIPTION_TT_TU_MN009_en.pdf
RF_TU_MN009	2-m relative humidity [%]	Hourly	106	v19.3	https://cdc.dwd.de/portal		https://cdc.dwd.de/sdi/pid/RF_TU_MN009/DESCRIPTION_RF_TU_MN009_en.pdf
F_MN003	10-m wind speed [m/s]	Hourly	57	v19.3	https://cdc.dwd.de/portal		https://cdc.dwd.de/sdi/pid/F_MN003/DESCRIPTION_F_MN003_en.pdf
D_MN003	10-m wind direction [deg]	Hourly	57	v19.3	https://cdc.dwd.de/portal		https://cdc.dwd.de/sdi/pid/D_MN003/DESCRIPTION_D_MN003_en.pdf
P0_MN008	surface pressure [hPa]	Hourly	38	v19.3	https://cdc.dwd.de/portal		https://cdc.dwd.de/sdi/pid/P0_MN008/DESCRIPTION_P0_MN008_en.pdf
R1_MN008	precipitation [mm]	Hourly	213	v19.3	https://cdc.dwd.de/portal		https://cdc.dwd.de/sdi/pid/R1_MN008/DESCRIPTION_R1_MN008_en.pdf
Hourly station observations of solar incoming (total/diffuse) and longwave downward radiation for Germany	Incoming longwave and shortwave radiation [J/cm2]	Hourly	10	recent	https://cdc.dwd.de/portal	24 May 2020	https://opendata.dwd.de/climate_environment/CDC/observations_germany/climate/hourly/solar//DESCRIPTION_obsgermany_climate_hourly_solar_en.pdf
MO_TT_MN004	2-m air temperature [°C]	Monthly	244	v19.3	https://cdc.dwd.de/portal		https://cdc.dwd.de/sdi/pid/MO_TT_MN004/DESCRIPTION_MO_TT_MN004_en.pdf
MODIS MYD11A1	land surface temperature [K]	Daily	--	v006	https://lpdaacsvc.cr.usgs.gov/appeears		https://lpdaac.usgs.gov/products/myd11a1v006/

465

Table 3: A summary of the statistical evaluation of the WRF_NO_NUDGE (italics) and WRF_NUDGE (bold italics) simulations, considering the whole evaluation period of 1 September 2017 to 1 September 2018. The table presents the mean deviation (MD), the mean absolute deviation (MAD) and the coefficient of determination (R^2) for two-hourly 2-m air temperature (*T*) and relative humidity *RH*), 10-m zonal wind (*U*) and meridional wind (*V*), surface pressure (*PS*), and daily total precipitation (*PR*). All computations are made from observations minus model data.

Variable	MD	MAD	R2
T (WRF_NO_NUDGE)	0.2	2.3	0.94
T (WRF_NUDGE)	**0.1**	**2.0**	**0.95**
RH	3.5	11.3	0.59
RH	**3.0**	**10.5**	**0.66**
U	0.1	1.5	0.48
U	**0.2**	**1.4**	**0.53**
V	0.2	1.2	0.35
V	**0.2**	**1.1**	**0.40**
PS	-0.7	2.2	0.97
PS	**-0.8**	**2.0**	**0.99**
PR	0.8	3.3	0.25
PR	**0.4**	**2.9**	**0.42**

Table 4: Same as Table 3 but for daily mean variables in WRF_NUDGE only.

Variable	MD	MAD	R2
T	**0.1**	**1.7**	**0.97**
RH	**3.0**	**8.4**	**0.71**
U	**0.2**	**0.9**	**0.72**
V	**0.2**	**0.6**	**0.64**
PS	**-0.8**	**2.0**	**0.99**